PHYSICS

# Interfacial charge transfer and persistent metallicity of ultrathin $SrIrO_3/SrRuO_3$ heterostructures

**Jocienne N. Nelson[1]†, Nathaniel J. Schreiber[2], Alexandru B. Georgescu[3,4], Berit H. Goodge[5], Brendan D. Faeth[1], Christopher T. Parzyck[1], Cyrus Zeledon[2]‡, Lena F. Kourkoutis[5,6], Andrew J. Millis[3,7], Antoine Georges[3,8,9,10], Darrell G. Schlom[2,6,11], Kyle M. Shen[1,6]***

**Interface quantum materials have yielded a plethora of previously unknown phenomena, including unconventional superconductivity, topological phases, and possible Majorana fermions. Typically, such states are detected at the interface between two insulating constituents by electrical transport, but whether either material is conducting, transport techniques become insensitive to interfacial properties. To overcome these limitations, we use angle-resolved photoemission spectroscopy and molecular beam epitaxy to reveal the electronic structure, charge transfer, doping profile, and carrier effective masses in a layer-by-layer fashion for the interface between the Dirac nodal-line semimetal $SrIrO_3$ and the correlated metallic Weyl ferromagnet $SrRuO_3$. We find that electrons are transferred from the $SrIrO_3$ to $SrRuO_3$, with an estimated screening length of $\lambda = 3.2 \pm 0.1$ Å. In addition, we find that metallicity is preserved even down to a single $SrIrO_3$ layer, where the dimensionality-driven metal-insulator transition typically observed in $SrIrO_3$ is avoided because of strong hybridization of the Ir and Ru $t_{2g}$ states.**

## INTRODUCTION

Ultrathin quantum materials present a unique platform for the control of electronic, magnetic, and topological properties. A commonly observed phenomenon in many ultrathin complex oxides and topological semimetals is that a crossover from a metallic to insulating state occurs below a critical thickness (*1*–*3*). This presents a potential challenge for realizing ultrathin heterostructures of quantum materials where metallic properties are desirable. Here, we show that this thickness-driven metal-insulator transition can be avoided even in the single unit cell limit in certain ultrathin oxide heterostructures.

We investigate the interface between $SrIrO_3$ and $SrRuO_3$, which has been of recent interest due to the observation of the topological Hall effect (*4*), suggesting the presence of skyrmions induced by Dzyaloshinskii-Moriya interactions (*5*), and may have potential for spintronic devices (*6*) due to the large spin Hall effect in $SrIrO_3$ (*7*). $SrRuO_3$ is a correlated Weyl ferromagnet (*8*), which gives rise to *k*-space magnetic monopoles in the Berry curvature (*9*) and for which a chiral anomaly has been recently reported (*10*). $SrIrO_3$ is a 5*d* Dirac nodal-line semimetal (*11*, *12*), formed through the confluence of strong spin-orbit interactions, Coulomb interaction, and octahedral rotations. The topological nature of $SrIrO_3$ and $SrRuO_3$ suggest that their properties will be sensitive to the location of the Fermi energy ($E_F$) with respect to the Dirac nodal line in $SrIrO_3$ or the Weyl points in $SrRuO_3$. Hole doping $SrIrO_3$, in particular, is an attractive target, because the nodal points are only 50 meV below $E_F$ but has been challenging to achieve in iridates through chemical substitution (*13*), thus interfacial charge transfer could be a promising alternative. Furthermore, the interplay of magnetism, spin-orbit coupling, electron correlations, and octahedral rotations make accurate theoretical predictions about the $SrIrO_3/SrRuO_3$ interface challenging.

In this work, heterostructures of *n* layers of $SrIrO_3$ are synthesized on bulk-like 20–unit cell–thick $SrRuO_3$ films by molecular beam epitaxy (MBE), where *n* is varied from 1 to 8. Using angle-resolved photoemission spectroscopy (ARPES), we investigate the evolution of the electronic structure of the topmost $SrIrO_3$ layer as it progresses away from the interface. Notably, a bulk-like metallic electronic structure is preserved down to the $n = 1$ limit, allowing us to isolate the impact of interfacial doping, where we find that approximately 0.5 electrons per Ir are transferred from the interfacial $SrIrO_3$ layer to $SrRuO_3$, shifting the $E_F$ of $SrIrO_3$ downward by approximately 80 meV and moving the Dirac node from below to above $E_F$. This charge transfer is confined within the first two unit cells of $SrIrO_3$, with an estimated screening length of $\lambda = 3.2 \pm 0.1$ Å. Last, the effective mass of the hole-like bands of $SrIrO_3$ are reduced with increased hole doping, revealing that the electronic structure of $SrIrO_3$ does not evolve in a perfectly rigid-band fashion.

## RESULTS

### Sample synthesis and characterization

$SrIrO_3/SrRuO_3$ heterostructures were synthesized by MBE. $SrRuO_3$ films were deposited on LSAT substrates, followed by *n* layers of $SrIrO_3$, described in Materials and Methods. Scanning transmission electron microscopy (STEM) images of $(SrIrO_3)_n/(SrRuO_3)_{20}$ heterostructures ($n = 1$ and 2) are shown in Fig. 1 (D and E), demonstrating precise control over the atomic thickness. After growth, samples were transferred through an ultrahigh vacuum manifold (pressure better than $10^{-10}$ torr) into an analysis chamber where ARPES, x-ray photoemission spectroscopy (XPS), and low-energy electron diffraction (LEED) measurements were performed. Figure 1A shows a

---

[1] Laboratory of Atomic and Solid State Physics, Department of Physics, Cornell University, Ithaca, NY 14853, USA. [2] Department of Materials Science and Engineering, Cornell University, Ithaca, NY 14853, USA. [3] Center for Computational Quantum Physics, Flatiron Institute, New York, NY 10010, USA. [4] Department of Materials Science and Engineering, Northwestern University, Evanston, IL 60208, USA. [5] School of Applied and Engineering Physics, Cornell University, Ithaca, NY 14853, USA. [6] Kavli Institute at Cornell for Nanoscale Science, Ithaca, NY 14853, USA. [7] Department of Physics, Columbia University, New York, NY 10027, USA. [8] Collège de France, 11 place Marcelin Berthelot, 75005 Paris, France. [9] CPHT, CNRS, Ecole Polytechnique, IP Paris, F-91128 Palaiseau, France. [10] DQMP, Universitè de Genéve, 24 quai Ernest Ansermet, CH-1211 Genéve, Suisse. [11] Leibniz-Institut für Kristallzüchtung, Max-Born-Str. 2, 12489 Berlin, Germany.
*Corresponding author. Email: kmshen@cornell.edu
†Present address: National Renewable Energy Laboratory, Golden, CO 80401, USA.
‡Present address: Pritzker School of Molecular Engineering, University of Chicago, Chicago, IL 60637, USA.

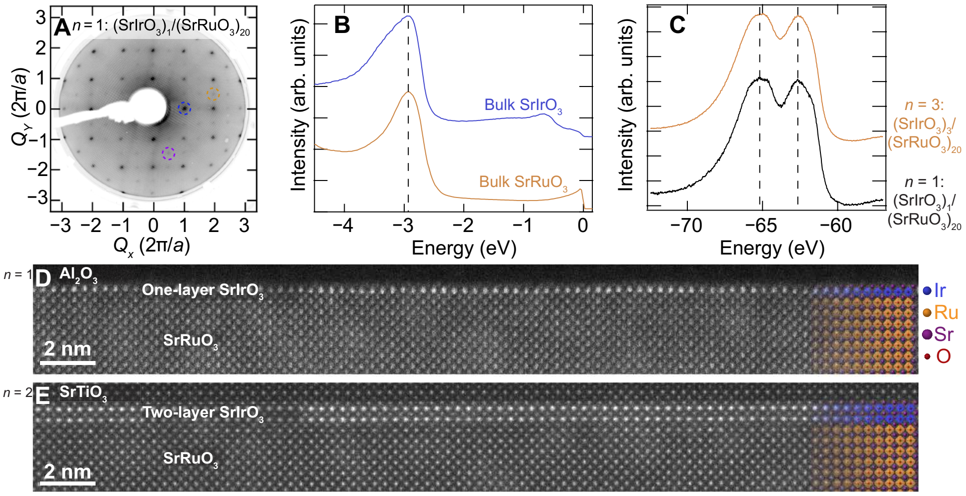

**Fig. 1. Interface between SrIrO$_3$ and SrRuO$_3$.** (**A**) LEED measurement of (SrIrO$_3$)$_1$/(SrRuO$_3$)$_{20}$ ($n = 1$) with 200-eV electrons at 35 K, with the blue circle highlighting the main cubic peaks, purple circle indicating peaks consistent with $\sqrt{2} \times \sqrt{2}$ $R45°$ octahedral rotations, and yellow circle indicating peaks corresponding to $c2 \times 2$ octahedral rotations. (**B**) Valence band spectra from bulk-like 24-nm-thick SrRuO$_3$ (yellow) and 8-nm-thick SrIrO$_3$ (blue) films. (**C**) XPS measurements of the Ir 4*f* core levels from $n = 1$ (black) and 3 (yellow), with dashed lines in (B) and (C) as guides to the eye. (**D** and **E**) High-angle annular dark-field scanning transmission electron microscopy (HAADF-STEM) images of $n = 1$ and 2 heterostructures measured along the $[100]_p$ direction, where *p* indicates the pseudocubic basis. This shows precise heterostructures with smooth and abrupt interfaces and with the SrIrO$_3$ layers terminated by the expected SrO layer. Samples were capped with either amorphous Al$_2$O$_3$ or crystalline SrTiO$_3$ following ARPES measurements but before removal from UHV.

LEED image of an $n = 1$ sample, demonstrating that the SrIrO$_3$ surface layer exhibits (0.5, 0.5), (±0.5, 0), and (0, ±0.5) diffraction spots (referenced in pseudocubic notation). This indicates that it has the same *Pnma* space group and octahedral rotation pattern ($a^-b^+a^-$, Glazer notation) as that of bulk (fig. S4) (*14*, *15*), although not necessarily with equal magnitude of rotations. In Fig. 1 (B and C), we show valence band and core level (XPS) measurements of the oxygen 2*p* and Ir 4*f* states, respectively. The difference in the relative position of the O 2*p* states has been used to estimate band alignment and charge transfer in oxide perovskite heterostructures (*16*), but here, the positions of the O 2*p* states in SrIrO$_3$ and SrRuO$_3$ appear to be nearly identical. Furthermore, there is little observable shift in the Ir 4*f* core levels as a function of the SrIrO$_3$ layer thickness. Therefore, inferring charge transfer between SrRuO$_3$ and SrIrO$_3$ appears to be beyond the capability of conventional core level and valence band spectroscopy used for estimating charge transfer in semiconductors (*17*). This suggests that only direct measurements of the near-$E_F$ electronic structure by ARPES can detect charge transfer at the heterointerface.

## ARPES measurements

In Fig. 2, we present the evolution of the electronic structure of (SrIrO$_3$)$_n$/(SrRuO$_3$)$_{20}$ as a function of *n*, as measured by ARPES. Because of the short photoelectron mean free path (<1 nm) (*18*), these measurements are predominantly sensitive to only the topmost SrIrO$_3$ layer, as evidenced by the fact that no distinct SrRuO$_3$ bands (fig. S5) (*19*) can be resolved in the near-$E_F$ ($E_B$ <1 eV) region, even for $n = 1$. The Fermi surface map of the $n = 8$ sample shows small electron pockets composed of Dirac fermions at (π/2,π/2) and heavy hole pockets at (π,0) (again defined in pseudocubic notation), effectively identical to previous ARPES measurements of thick, bulk-like films of SrIrO$_3$ (*15*) and in good agreement with density functional theory (DFT) calculations [$k_z = 0.5\pi/c$, consistent with (*15*)]. We note that the features centered at (0,0) and (π,π) shows weak photoemission intensity likely due to matrix element effects but are present in the ARPES data. With increasing binding energy, the electron pockets shrink and disappear, while the hole pockets expand as determined from intermediate energies and the *E* versus *k* dispersion. At $E_B = 80$ meV, because of the weak spectral intensity from the bands that are back-folded because of the bulk in-plane octahedral rotations, this approximates a circular contour. However, as highlighted in white (Fig. 2), the map actually consists purely of square hole pockets. This qualitative behavior is reproduced in the DFT calculations at higher binding energies when taking into account a mass renormalization ($m^*/m_b$) of 2, consistent with prior dynamical mean field theory calculations (*20*). This correction is estimated on the basis of the velocity of the linear Dirac dispersion, which forms the electron pockets centered at (π/2,π/2), where $v_{F,DFT} \sim 2v_F$. We compare DFT and ARPES using the empirical formula $E_B = \frac{E_{DFT}}{2} - 0.035$ eV, which allows for reasonable agreement between DFT and ARPES on the size of the electron and hole pockets at each binding energy. Similar features are also observed for $n = 3$ (also $n = 5$; see fig. S6), suggesting that an undoped bulk-like electronic structure persists down to 3 SrIrO$_3$ pseudocubic unit cells from the SrRuO$_3$ interface. In contrast, ARPES spectra from $n = 1$ exhibits a notable departure from the bulk-like $n \geq 3$ heterostructures, with a distinctive FS at $E_F$ that is nearly identical to the intensity maps of bulk-like $n \geq 3$ at a binding energy of $E_B = 80$ meV, indicating a downward shift of the chemical potential, Δμ, as the SrRuO$_3$ interface is approached with preservation of the bulk-like metallic SrIrO$_3$ state. Notably, no evidence of any gap or suppression of the spectral weight is observed in the $n = 1$ sample (Fig. 4E), as might be expected for quasi–two-dimensional iridates, such as the Mott-insulating Sr$_2$IrO$_4$. The $n = 2$ heterostructure exhibits behavior intermediate between $n = 1$ and 3. This shifting Δμ with decreasing *n* is also supported by the similarity of the intensity pattern at even higher binding energies (bottom row), where the intensity pattern at $E_B = 370$ meV for the bulk-like $n = 8$ sample is closely

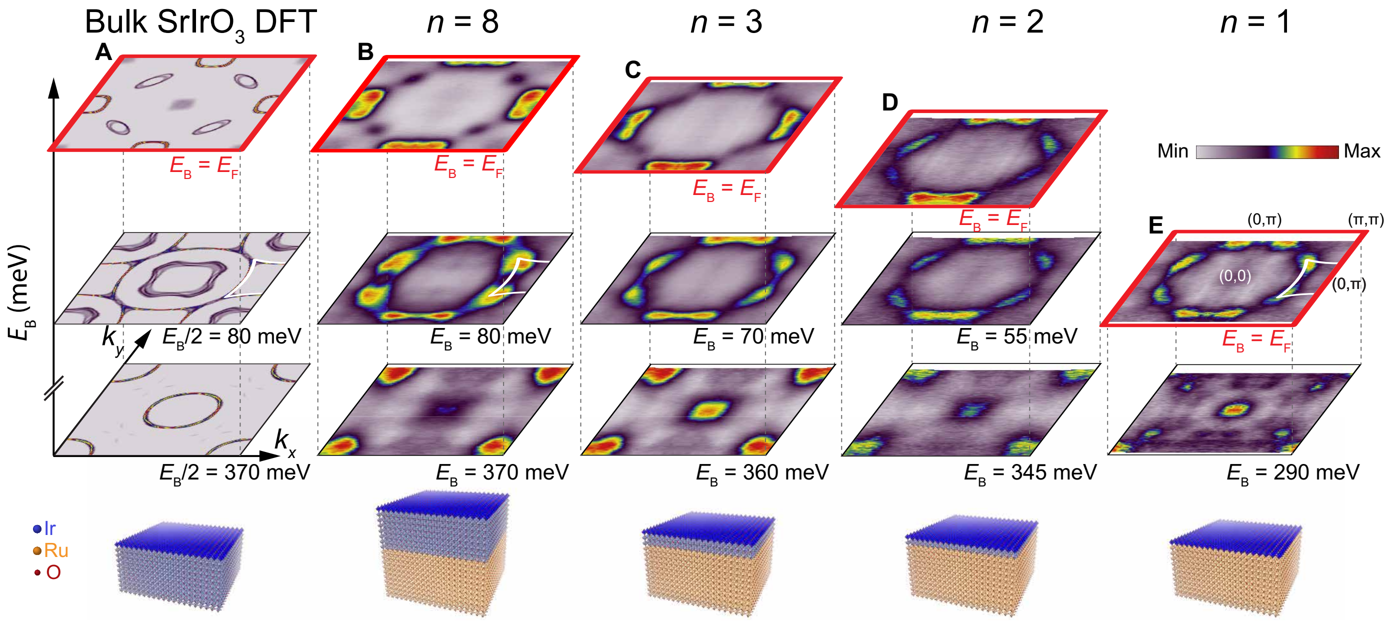

**Fig. 2. Constant energy intensity ARPES maps of $(SrIrO_3)_n/(SrRuO_3)_{20}$ heterostructures.** (**A**) Density functional theory (DFT) calculations of constant energy intensity maps for bulk $SrIrO_3$ at a variety of binding energies, $k_z = 0.5\ \pi/c$. The binding energies are renormalized by a factor of 2 to account for many body effects described in the text. The conversion between experiment and DFT is $E_B = E_{DFT}/2 - 0.035$ eV. (**B** to **E**) ARPES intensity maps for the $n = 8$, 3, 2, and 1 heterostructures, with the top row showing the Fermi surface at $E_B = E_F$ highlighted in red. The square hole pockets are highlighted in white as a guide to the eye in the 80 meV maps of the DFT, $n = 8$ and the FS of the $n = 1$, demonstrating that the map consists purely of hole pockets. All data are presented in the pseudocubic Brillouin zone (i.e., 1 Ir per unit cell) and symmetrized about $k_x = 0$; unsymmetrized data are shown in fig. S6.

reproduced at $E_B = 370 - \Delta\mu = 290$ meV for $n = 1$. We also note that the extremely strong similarity between the $n = 1$ and shifted $n = 8$ maps indicates that the electronic states for the single $SrIrO_3$ layer for $n = 1$ retains a character very similar to the bulk-like, three-dimensional electronic structure seen in the $n = 8$ sample. This may appear counterintuitive, because it might be expected that ultrathin $SrIrO_3$ should exhibit a quasi–two-dimensional insulating electronic structure similar to $Sr_2IrO_4$. As we will describe later, such quantum confinement is avoided because of hybridization between the $SrIrO_3$ and $SrRuO_3$ $t_{2g}$ states. Such hybridization between the Ru and Ir states is indicated in our orbitally projected DFT calculations of a $SrIrO_3/SrRuO_3$ superlattice. For example, orbitally projected FS calculations (fig. S9) clearly show features with clearly mixed Ru and Ir character. In particular, the small "dot" of spectral weight at (0,0) in the $n = 1$ data appears to be of predominantly Ru character, based on the comparison to the calculations. In addition, some of the spectral weight between (0,0) and (π,π) in the $n = 1$ sample at $E_B = 290$ meV is not predicted to occur in bulk $SrIrO_3$ and thus should likely arise from hybridization with the $SrRuO_3$. Together, these measurements strongly suggest that the effect of the $SrRuO_3$ is to hole dope the iridate layer and that the interface consists of electronically distinct layers and is not an alloyed system, also suggested by the abrupt interfaces seen by STEM in Fig. 1 (D and E). Because the ARPES measurements are sensitive to only the topmost $SrIrO_3$ layer of the heterostructure, this series of measurements can be thought of as effectively a layer-by-layer tomographic reconstruction of the electronic structure and charge transfer at the $SrIrO_3$-$SrRuO_3$ interface.

In Fig. 3 we shown the shift of Δμ as a function of thickness extracted from the ARPES maps in Fig. 2. By fitting to an exponential, we find that the chemical potential shift due to charge transfer between $SrIrO_3$ and $SrRuO_3$ can be well described by the empirical function $\Delta\mu \propto e^{-d/\lambda}$, where $d$ is the thickness of the $SrIrO_3$ layers and the screening length is $\lambda = 3.2 \pm 0.1$ Å. While this precise number may be affected by nonrigid band effects that we will detail later, this clearly demonstrates the very short length scale of charge transfer in this correlated oxide system, which is relevant for designing ultrathin electronics. The amount of hole doping, $\Delta h^+(n)$, can also be estimated by shifting the chemical potential in the DFT calculations by the experimentally determined Δμ (taking into account the mass renormalization factor $v_{F,DFT} \sim 2v_F$), shown in Fig. 3A. The rapid decay of Δμ (and $\Delta h^+$) indicates that, above three layers away from the interface, there is no appreciable amount of charge transfer, as shown in Fig. 3A. Here, charge transfer is not used in typical sense of transfer across a buried interface; instead, it describes the estimated doping of the topmost $SrIrO_3$ probed by ARPES. However, it is a closely related quantity, and while the exact $\Delta\mu(n)$ may change slightly in a buried interface between bulk-like $SrIrO_3$ and $SrRuO_3$, the magnitude and direction of charge transfer should hold. Even the angular distribution of ARPES intensity around a circular path through the FS of $n = 1$ matches quantitatively to that of $n = 8$ at $E_B = 80$ meV. This is shown in Fig. 3B, where the distinctive eight-lobed intensity pattern is plotted as a function of polar angle around the FS.

In Fig. 4 (A to D), we show ARPES spectra along two high-symmetry directions for the doped $n = 1$ and undoped $n = 8$ heterostructures. Energy distribution curves at the Fermi crossings shown in Fig. 4E show strong spectral weight at $E_F$, further demonstrating the persistent metallic nature of the $n = 1$ heterostructure. At a qualitative level, the change from $n = 1$ to 8 can be well described by

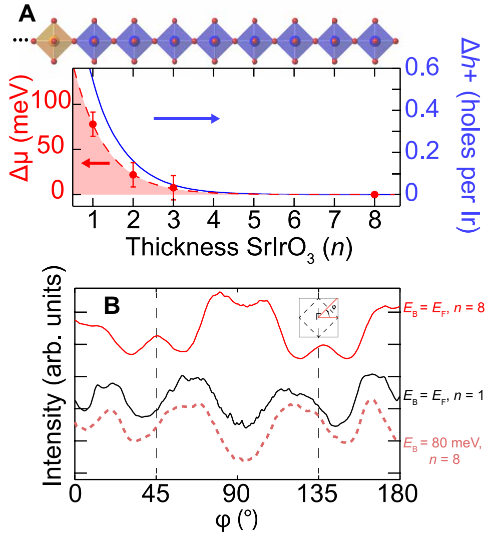

**Fig. 3. Charge transfer and chemical potential shift at SrIrO$_3$-SrRuO$_3$ interface.** (**A**) Dependence of the shift of the chemical potential (red) and carrier concentration calculated by DFT (blue) on thickness. This illustrates that the $n \geq 3$ samples are approximately bulk like. (**B**) Intensity integrated along a circular path around the FS for the $n = 8$ sample (red solid lines), which is shifted vertically for clarity; this contrasts with the integrated intensity from the $n = 1$ FS (black) and the $n = 8$, $E_B = 80$ meV constant energy map (pink dashed lines), which display a similar angular dependence. The inset shows the Brillouin zone with the angle φ defined.

a shift of $\Delta\mu = 80$ meV, consistent with Fig. 3. This chemical potential shift pushes the Dirac node at $(\pi/2,\pi/2)$ (located 50 meV below $E_F$ in bulk) slightly above $E_F$ for $n = 1$. The ability to shift the Dirac node closer to $E_F$ without substitutional disorder could be a promising approach to achieve very high mobilities in SrIrO$_3$, as has been demonstrated in its sister compound, CaIrO$_3$ (*21*), where mobilities greater than 60,000 cm$^2$ V$^{-1}$ s$^{-1}$ have been reported, ostensibly because of the proximity of the Dirac node to $E_F$ (*22*). Nevertheless, a more detailed analysis of the hole pocket clearly shows that the electronic structure does not evolve purely in a simple, rigid-band fashion. In Fig. 4F, the dispersions around $(0,\pi)$-$(0,0)$ are plotted as a function of $n$, along with parabolic fits that are vertically shifted to match the top of the parabolas. This clearly demonstrates that the extracted effective mass, $m^*$ ($E = E_0 - \hbar^2k^2/2m^*$), decreases by nearly half when going from the bulk-like $n = 8$ heterostructure ($m^* = 1.6 \pm 0.2 m_e$) to the single layer $n = 1$ heterostructure ($m_1^* = 0.8 \pm 0.1\, m_e$), summarized in Fig. 4G. We note that the effective mass of this band along this in-plane direction changes only by 6% as a function of $k_z$ throughout the Brillouin zone.

## DISCUSSION

As has now been well established, the rich electronic and magnetic properties of the iridates arise from a complex interplay of spin-orbit coupling, electron correlations, octahedral rotations, and dimensionality. Insulating behavior is generally observed in other quasi–two-dimensional iridates such as Sr$_2$IrO$_4$ and Sr$_3$Ir$_2$O$_7$ (*23*, *24*) as well as in thin-film heterostructures such as ultrathin SrIrO$_3$ on SrTiO$_3$ (*25*, *26*) or SrIrO$_3$-SrTiO$_3$ superlattices (*27*, *28*), raising the obvious question as to why our ultrathin SrIrO$_3$ heterostructure retain a highly metallic character, even for $n = 1$. The key distinction is that, in the prior examples, the Ir 5*d* states are confined to two dimensions, either by double SrO rock salt layers or by an insulating SrTiO$_3$ substrate/blocking layers. In contrast, here, the SrRuO$_3$ "substrate" is highly metallic with similar near-$E_F$ $t_{2g}$ states that hybridize with the SrIrO$_3$ electronic states (*11*, *29*). This prevents quantum confinement, which requires the substrate to have a gap in the available density of states with which the SrIrO$_3$ states could hybridize, either in an insulator with a full bandgap (e.g., SrTiO$_3$), a material with a gap along the film-substrate direction [(e.g., Ag/Au(111) heterostructures (*30*))] or from orbital symmetry considerations (*30*). In this way, although for $n = 1$ the SrIrO$_3$ layer is only a single unit cell thick from a structural and chemical perspective, its electronic wave function nevertheless retains a three-dimensional bulk-like character due to its extending into the SrRuO$_3$ layers beneath.

The hybridization of the Ir 5*d* states with the Ru $t_{2g}$ states and subsequent preserved three-dimensionality not only explains why a dimensionality-driven metal-insulator transition is avoided but also explains the strong similarity of the ARPES spectra from the $n = 1$ heterostructure to the thicker, bulk-like samples. For instance, the FS map of the $n = 1$ sample is nearly identical to the ARPES intensity map from the bulk-like $n = 8$ sample at $E_B = 80$ meV. However, if the Ir 5*d* states were confined to two dimensions, then the $n = 1$ or 2 samples should have a radically different electronic structure than bulk SrIrO$_3$, perhaps more closely resembling doped Sr$_2$IrO$_4$ or Sr$_3$Ir$_2$O$_7$ (*13*, *31*–*33*). Our experimental observations are therefore entirely consistent with a three-dimensional bulk-like electronic structure being preserved even in the $n = 1$ limit. Furthermore, because the terminating layer is SrIrO$_3$ for all heterostructures, the work function and thus the inner potential and probed $k_z$ value ($k_z = 0.5\ \pi/c$) should be the same across all samples, consistent with our experimental observations.

In iridates, it has been established that the octahedral rotations and tilts are also strongly related to the electronic structure through the large spin-orbit coupling. Because SrRuO$_3$ exhibits a similar lattice constant as SrIrO$_3$, the strain is minimized, and the octahedral rotations in SrIrO$_3$ should be much less perturbed than on materials that impart substantial strain (e.g., SrTiO$_3$). This is evidenced by the LEED patterns for all samples remaining unchanged from bulk all the way down to $n = 1$ (Fig. 1 and fig. S4), suggesting that both bulk SrIrO$_3$ and (SrIrO$_3$)$_1$/(SrRuO$_3$)$_{20}$ have the same pattern of octahedral rotations as bulk. This is likewise consistent with our DFT calculations for a (SrRuO$_3$)$_1$/(SrIrO$_3$)$_1$ superlattice, which displayed very minor changes in bond angles (<1°) relative to bulk SrIrO$_3$ (note S3). Last, because both SrIrO$_3$ and SrRuO$_3$ are nonpolar, the possibility of a polar reconstruction at the interface (e.g., LaAlO$_3$/SrTiO$_3$) can be eliminated.

Therefore, having ruled out quantum confinement/dimensionality, structural modification, and polar discontinuity effects as possibilities, we can then conclude that the observed interfacial charge transfer should be driven by the inherent band alignment between SrIrO$_3$ and SrRuO$_3$. This is consistent with comparisons of the Schottky barrier heights of the SrRuO$_3$/Nb:SrTiO$_3$(001) (*34*) and SrIrO$_3$/Nb:SrTiO$_3$(001) (*35*), which indicate a small (≈30 meV) difference in work functions that would imply a transfer of electrons from the Ir to Ru layers. This is also consistent with the aforementioned DFT calculations on a (SrRuO$_3$)$_1$/(SrIrO$_3$)$_1$ superlattice (fig. S8), which also indicate a transfer of electrons from the Ir to the Ru layers. While these differences in work function and charge transfer by DFT are qualitatively consistent with our own conclusions, they are

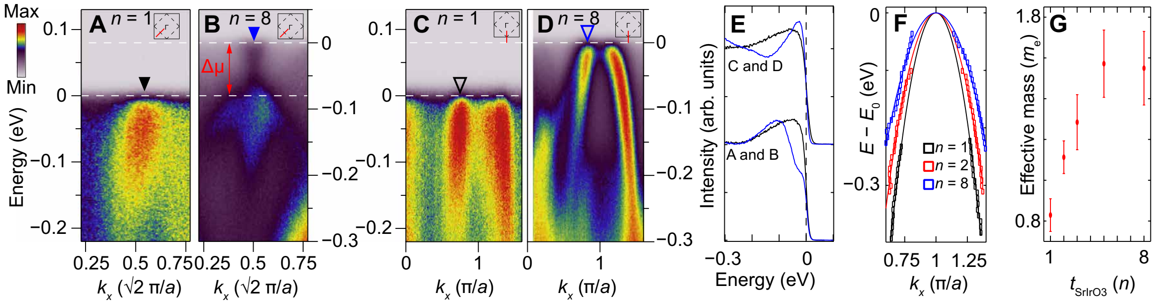

**Fig. 4. Evolution of quasiparticle dispersion and effective mass with *n*.** (**A** and **B**) Dispersion along (0,0)-(π,π) for $n = 1$ and 8 showing the shifting of the Dirac cone in bulk to above $E_F$ for $n = 1$. (**C** and **D**) Dispersion along (0,0)-(0,π) for $n = 1$ and 8 showing the evolution of the quasiparticle dispersion of the hole-like bands. (**E**) Energy distribution curves at the Fermi crossings in (A) to (D) as indicated by the black and blue triangles. (**F**) Extracted dispersion along (0,0)-(0,π) for $n = 1$, 2, and 8 together with a parabolic fit used to extract $m^*$ from the curvature; dispersions are plotted relative to the band maximum. (**G**) Evolution of $m^*$ with $n$.

also sufficiently small to underscore the need for high-resolution ARPES to provide a clear picture of the evolution of the electronic structure at the interface.

In summary, we have demonstrated a powerful approach for elucidating the evolution of the low-energy interfacial electron structure in a layer-by-layer fashion in correlated metallic heterostructures using ARPES. Our work reveals that electrons are transferred from $SrIrO_3$ to $SrRuO_3$, resulting in hole doping of the closest two $SrIrO_3$ layers to the $SrIrO_3$-$SrRuO_3$ interface, which may have implications to their topological and low-energy properties by pushing the Dirac node of $SrIrO_3$ close to $E_F$. Furthermore, we reveal that ultrathin layers of $SrIrO_3$ on $SrRuO_3$ unexpectedly do not exhibit a crossover to insulating behavior, as has been observed in layered iridates ($Sr_2IrO_4$ and $Sr_3Ir_2O_7$) or ultrathin heterostructures ($SrIrO_3$ on $SrTiO_3$ and $SrIrO_3$-$SrTiO_3$ superlattices), due to the strong hybridization of the Ir and Ru $t_{2g}$ states. The enhanced metallicity (higher carrier density and lower effective mass) of a single unit cell of $SrIrO_3$ on $SrRuO_3$ is notable, given that it runs counter to the typical trend where metallicity is suppressed in ultrathin complex oxides and topological semimetals on insulating substrates [e.g., $LaNiO_3$ (*1*), $SrRuO_3$ (*36*), and $Cd_3As_2$ (*2*)]. The enhanced screening for $n = 1$, potentially arising both from the increased carrier density in the Ir 5*d* orbitals and the highly metallic $SrRuO_3$, could be responsible for the reduced $m^*$, and possibly a decrease in the effective strength of electron correlations, possibly explaining why the interfacial $SrIrO_3$ layers do not evolve in a perfectly rigid-band fashion. This opens a new avenue for engineering the properties of complex oxides, topological semimetals, and other quantum materials in the ultrathin limit through the judicious selection of the appropriate interface properties and density of states.

## MATERIALS AND METHODS

### Thin-film growth

Epitaxial $SrRuO_3$ thin films 20 layers (approximately 8 nm) thick were grown using a Veeco GEN10 MBE system on single crystalline LSAT substrates at a substrate temperature of 650°C as measured by an optical pyrometer with a measurement wavelength of 1550 nm in a background partial pressure of $4 \times 10^{-6}$ torr of distilled ozone (80% $O_3$ + 20% $O_2$). Strontium was evaporated using a low-temperature effusion cell at a flux of $1.5 \times 10^{13}$ atom cm$^{-2}$ s$^{-1}$, while ruthenium was evaporated using an electron beam evaporator. Strontium and ruthenium were codeposited with a Ru/Sr atomic ratio of 1.7-2 starting with an initial nucleation layer of one SrO monolayer before codepositing to avoid formation of ruthenium metal at the interface. Films were then transported in air to a second Veeco GEN10 MBE chamber, where a pristine surface was recovered by annealing the films at 300°C in a background partial pressure of $1 \times 10^{-6}$ torr of distilled ozone (80% $O_3$ + 20% $O_2$) for 30 min (*37*). Subsequently, the substrate temperature was raised to 660°C (measured by an optical pyrometer with $\lambda = 980$ nm) for the growth of the $SrIrO_3$ layer. Strontium was supplied by a low-temperature effusion cell using a flux of $3 \times 10^{12}$ to $1.3 \times 10^{13}$ atom cm$^{-2}$ s$^{-1}$, and iridium was supplied using an electron beam evaporator. Strontium and iridium were codeposited with an Ir/Sr ratio of 1.2-1.7. All films were capped following measurement before removal from ultrahigh vacuum (UHV) by either amorphous $Al_2O_3$ or crystalline $SrTiO_3$. Additional details about the growth and sample characterization may be found in (*15*, *38*) and note S1.

### Photoemission measurements

Following $SrIrO_3$ growth, the samples were immediately transferred through a UHV manifold (pressures better than $10^{-10}$ torr) to an analysis chamber, where high-resolution ARPES measurements were performed using a VG Scienta R4000 electron analyzer and a VUV5000 helium plasma discharge lamp and monochromator. He Iα ($h\nu = 21.2$ eV) photons with an energy resolution of $\Delta E = 11$ meV at a temperature of 15 K were used unless otherwise noted. XPS measurements were performed immediately after ARPES measurements in the same vacuum chamber using a Scienta Omicron DAR 400 twin anode Mg/Al x-ray source using Mg Kα $h\nu = 1253.6$ eV photons with an energy resolution of $\Delta E = 0.625$ eV. LEED measurements were performed using a four-grid LEED optics (SPECS ErLEED 150) in a reflection geometry.

### STEM images

Cross-sectional STEM specimens were prepared using the standard focused ion beam (FIB) lift-out process on Thermo Scientific Helios G4 UX FIB or an FEI Strata 400 FIB equipped with an OmniProbe AutoProbe 200 nanomanipulator. High-angle annular dark-field STEM (HAADF-STEM) images were acquired on an aberration-corrected 300 keV FEI Titan Themis with a probe convergence semiangle of 21.4 mrad and inner and outer collection angles of 68 and 340 mrad, respectively.

## DFT calculations

The calculations were performed using Quantum ESPRESSO. The structures were relaxed imposing in-plane 1.8% compressive lattice strain along the *xy* direction relative to the freely relaxed bulk $SrIrO_3$. The final electronic calculations are performed using projector augmented wave pseudopotentials, using the Perdew-Burke-Ernzerhof functional and including spin-orbit coupling, a *k*-mesh of 10 × 10 × 8, and 816 eV plane wave cutoff. We did not include an additional Hubbard *U*, as both previous work (*15*) and our own has found that it is not necessary to reproduce the main features of the FS of bulk $SrIrO_3$. To obtain the layer-projected FS, we performed a Wannierization of the Ru and Ir $t_{2g}$ states around the Fermi level using Wannier90. Our calculated FSs are then obtained by projecting only the Ir $t_{2g}$ atoms onto the FS. To best simulate the FS, we found a $k_z = 0.5\ \pi/c$ to be optimal, in agreement with previous work (*15*), and use an energy renormalization of $E_{\mathrm{B}} = \frac{E_{\mathrm{DFT}}}{2} - 0.035$ eV. We found that the $(SrRuO_3)_1/(SrIrO_3)_1$ superlattice adequately reproduces the main features of the FS. To simulate the $(SrRuO_3)_1/(SrIrO_3)_1$ superlattice and bulk $SrIrO_3$, we performed 20 atom $c(2 \times 2) \times 2$ unit cell calculations. While we did perform slab calculations including one layer of $SrIrO_3$ followed by five layers of $SrRuO_3$ and vacuum, these were not as easy to interpret in a layer-by-layer basis because of the large number of Wannier functions and their relatively delocalized nature.

## SUPPLEMENTARY MATERIALS

Supplementary material for this article is available at https://science.org/doi/10.1126/sciadv.abj0481

## REFERENCES AND NOTES

1. P. D. C. King, H. I. Wei, Y. F. Nie, M. Uchida, C. Adamo, S. Zhu, X. He, I. Bozovic, D. G. Schlom, K. M. Shen, Atomic-scale control of competing electronic phases in ultrathin $LaNiO_3$. *Nat. Nanotechnol.* **9**, 443–447 (2014).
2. Z. Wang, H. Weng, Q. Wu, X. Dai, Z. Fang, Three-dimensional dirac semimetal and quantum transport in $Cd_3As_2$. *Phys. Rev. B* **88**, 125427 (2013).
3. M. Huijben, L. W. Martin, Y.-H. Chu, M. B. Holcomb, P. Yu, G. Rijnders, D. H. A. Blank, R. Ramesh, Critical thickness and orbital ordering in ultrathin $La_{0.7}Sr_{0.3}MnO_3$ films. *Phys. Rev. B* **78**, 094413 (2008).
4. J. Matsuno, N. Ogawa, K. Yasuda, F. Kagawa, W. Koshibae, N. Nagaosa, Y. Tokura, M. Kawasaki, Interface-driven topological Hall effect in $SrRuO_3$-$SrIrO_3$ bilayer. *Sci. Adv.* **2**, e1600304 (2016).
5. K.-Y. Meng, A. S. Ahmed, M. Baćani, A.-O. Mandru, X. Zhao, N. Bagués, B. D. Esser, J. Flores, D. W. McComb, H. J. Hug, F. Yang, Observation of nanoscale skyrmions in $SrIrO_3/SrRuO_3$ bilayers. *Nano Lett.* **19**, 3169–3175 (2019).
6. L. Liu, Q. Qin, W. Lin, C. Li, Q. Xie, S. He, X. Shu, C. Zhou, Z. Lim, J. Yu, W. Lu, M. Li, X. Yan, S. J. Pennycook, J. Chen, Current-induced magnetization switching in all-oxide heterostructures. *Nat. Nanotechnol.* **14**, 939–944 (2019).
7. A. S. Patri, K. Hwang, H.-W. Lee, Y. B. Kim, Theory of large intrinsic spin hall effect in iridate semimetals. *Sci. Rep.* **8**, 8052 (2018).
8. Y. Chen, D. L. Bergman, A. A. Burkov, Weyl fermions and the anomalous hall effect in metallic ferromagnets. *Phys. Rev. B* **88**, 125110 (2013).
9. Z. Fang, N. Nagaosa, K. S. Takahashi, A. Asamitsu, R. Mathieu, T. Ogasawara, H. Yamada, M. Kawasaki, Y. Tokura, K. Terakura, The anomalous hall effect and magnetic monopoles in momentum space. *Science* **302**, 92–95 (2003).
10. K. Takiguchi, Y. K. Wakabayashi, H. Irie, Y. Krockenberger, T. Otsuka, H. Sawada, S. A. Nikolaev, H. Das, M. Tanaka, Y. Taniyasu, H. Yamamoto, Quantum transport evidence of Weyl fermions in an epitaxial ferromagnetic oxide. *Nat. Commun.* **11**, 4969 (2020).
11. J.-M. Carter, V. V. Shankar, M. A. Zeb, H.-Y. Kee, Semimetal and topological insulator in perovskite iridates. *Phys. Rev. B* **85**, 115105 (2012).
12. C. Fang, Y. Chen, H.-Y. Kee, L. Fu, Topological nodal line semimetals with and without spinorbital coupling. *Phys. Rev. B* **92**, 081201 (2015).
13. J. N. Nelson, C. T. Parzyck, B. D. Faeth, J. K. Kawasaki, D. G. Schlom, K. M. Shen, Mott gap collapse in lightly hole-doped $Sr_{2-x}K_xIrO_4$. *Nat. Commun.* **11**, 2597 (2020).
14. J. G. Zhao, L. X. Yang, Y. Yu, F. Y. Li, R. C. Yu, Z. Fang, L. C. Chen, C. Q. Jin, High-pressure synthesis of orthorhombic $SrIrO_3$ perovskite and its positive magnetoresistance. *J. Appl. Phys.* **103**, 103706 (2008).
15. Y. F. Nie, P. D. C. King, C. H. Kim, M. Uchida, H. I. Wei, B. D. Faeth, J. P. Ruf, J. P. C. Ruff, L. Xie, X. Pan, C. J. Fennie, D. G. Schlom, K. M. Shen, Interplay of spin-orbit interactions, dimensionality, and octahedral rotations in semimetallic $SrIrO_3$. *Phys. Rev. Lett.* **114**, 016401 (2015).
16. Z. Zhong, P. Hansmann, Band alignment and charge transfer in complex oxide interfaces. *Phys. Rev. X* **7**, 011023 (2017).
17. J. R. Waldrop, R. W. Grant, S. P. Kowalczyk, E. A. Kraut, Measurement of semiconductor heterojunction band discontinuities by x-ray photoemission spectroscopy. *J. Vac. Sci. Technol* **3**, 835–841 (1985).
18. M. P. Seah, W. A. Dench, Quantitative electron spectroscopy of surfaces: A standard data base for electron inelastic mean free paths in solids. *Surf. Interface Anal.* **1**, 2–11 (1979).
19. D. E. Shai, C. Adamo, D. W. Shen, C. M. Brooks, J. W. Harter, E. J. Monkman, B. Burganov, D. G. Schlom, K. M. Shen, Quasiparticle mass enhancement and temperature dependence of the electronic structure of ferromagnetic $SrRuO_3$ thin films. *Phys. Rev. Lett.* **110**, 087004 (2013).
20. H. Zhang, K. Haule, D. Vanderbilt, Effective *j*=1/2 insulating state in ruddlesden-popper iridates: An LDA+DMFT study. *Phys. Rev. Lett.* **111**, 246402 (2013).
21. R. Yamada, J. Fujioka, M. Kawamura, S. Sakai, M. Hirayama, R. Arita, T. Okawa, D. Hashizume, M. Hoshino, Y. Tokura, Large variation of dirac semimetal state in perovskite $CaIrO_3$ with pressure-tuning of electron correlation. *Phys. Rev. Lett.* **123**, 216601 (2019).
22. J. Fujioka, R. Yamada, M. Kawamura, S. Sakai, M. Hirayama, R. Arita, T. Okawa, D. Hashizume, M. Hoshino, Y. Tokura, Strong-correlation induced high-mobility electrons in Dirac semimetal of perovskite oxide. *Nat. Commun.* **10**, 362 (2019).
23. B. J. Kim, H. Jin, S. J. Moon, J.-Y. Kim, B.-G. Park, C. S. Leem, J. Yu, T. W. Noh, C. Kim, S.-J. Oh, J.-H. Park, V. Durairaj, G. Cao, E. Rotenberg, Novel $J_{\mathrm{eff}} = 1/2$ Mott state induced by relativistic spin-orbit coupling in $Sr_2IrO_4$. *Phys. Rev. Lett.* **101**, 076402 (2008).
24. B. M. Wojek, M. H. Berntsen, S. Boseggia, A. T. Boothroyd, D. Prabhakaran, D. F. McMorrow, H. M. Rønnow, J. Chang, O. Tjernberg, The $J_{\mathrm{eff}} = 1/2$ insulator $Sr_3Ir_2O_7$ studied by means of angle-resolved photoemission spectroscopy. *J. Phys. Condens. Matter* **24**, 415602 (2012).
25. W. Guo, D. X. Ji, Z. B. Gu, J. Zhou, Y. F. Nie, X. Q. Pan, Engineering of octahedral rotations and electronic structure in ultrathin $SrIrO_3$ films. *Phys. Rev. B* **101**, 085101 (2020).
26. P. Schütz, D. Di Sante, L. Dudy, J. Gabel, M. Stübinger, M. Kamp, Y. Huang, M. Capone, M.-A. Husanu, V. N. Strocov, G. Sangiovanni, M. Sing, R. Claessen, Dimensionality-driven metal-insulator transition in spin-orbit-coupled $SrIrO_3$. *Phys. Rev. Lett.* **119**, 256404 (2017).
27. J. Matsuno, K. Ihara, S. Yamamura, H. Wadati, K. Ishii, V. V. Shankar, H.-Y. Kee, H. Takagi, Engineering a spin-orbital magnetic insulator by tailoring superlattices. *Phys. Rev. Lett.* **114**, 247209 (2015).
28. L. Hao, D. Meyers, C. Frederick, G. Fabbris, J. Yang, N. Traynor, L. Horak, D. Kriegner, Y. Choi, J.-W. Kim, D. Haskel, P. J. Ryan, M. P. M. Dean, J. Liu, Two-dimensional $J_{\mathrm{eff}} = 1/2$ antiferromagnetic insulator unraveled from interlayer exchange coupling in artificial perovskite iridate superlattices. *Phys. Rev. Lett.* **119**, 027204 (2017).
29. H.-T. Jeng, S.-H. Lin, C.-S. Hsue, Orbital ordering and Jahn-Teller distortion in perovskite ruthenate $SrRuO_3$. *Phys. Rev. Lett.* **97**, 067002 (2006).
30. T.-C. Chiang, Photoemission studies of quantum well states in thin films. *Surf. Sci. Rep.* **39**, 181–235 (2000).
31. Y. Cao, Q. Wang, J. A. Waugh, T. J. Reber, H. Li, X. Zhou, S. Parham, S.-R. Park, N. C. Plumb, E. Rotenberg, A. Bostwick, J. D. Denlinger, T. Qi, M. A. Hermele, G. Cao, D. S. Dessau, Hallmarks of the Mott-metal crossover in the hole-doped pseudospin-1/2 Mott insulator $Sr_2IrO_4$. *Nat. Commun.* **7**, 11367 (2016).
32. V. Brouet, L. Serrier-Garcia, A. Louat, L. Fruchter, F. Bertran, P. Le Fevre, J. Rault, A. Forget, D. Colson, Coherent and incoherent bands in La and Rh doped $Sr_3Ir_2O_7$. *Phys. Rev. B* **98**, 235101 (2018).
33. J. L. Schmehr, T. R. Mion, Z. Porter, M. Aling, H. Cao, M. H. Upton, Z. Islam, R.-H. He, R. Sensarma, N. Trivedi, S. D. Wilson, Overdamped antiferromagnetic strange metal state in $Sr_3IrRuO_7$. *Phys. Rev. Lett.* **122**, 157201 (2019).
34. Y. Hikita, Y. Kozuka, T. Susaki, H. Takagi, H. Y. Hwang, Characterization of the Schottky barrier in $SrRuO_3$/Nb:$SrTiO_3$ junctions. *Appl. Phys. Lett.* **90**, 143507 (2007).
35. B. S. Y. Kim, Y. A. Birkholzer, X. Feng, Y. Hikita, H. Y. Hwang, Probing the band alignment in rectifying $SrIrO_3$/Nb:$SrTiO_3$ heterostructures. *Appl. Phys. Lett.* **114**, 133504 (2019).
36. J. Xia, W. Siemons, G. Koster, M. R. Beasley, A. Kapitulnik, Critical thickness for itinerant ferromagnetism in ultrathin films of $SrRuO_3$. *Phys. Rev. B* **79**, 140407 (2009).
37. J. Shin, S. V. Kalinin, H. N. Lee, H. M. Christen, R. G. Moore, E. W. Plummer, A. P. Baddorf, Surface stability of epitaxial $SrRuO_3$ films. *Surf. Sci.* **581**, 118–132 (2005).
38. H. P. Nair, Y. Liu, J. P. Ruf, N. J. Schreiber, S.-L. Shang, D. J. Baek, B. H. Goodge, L. F. Kourkoutis, Z.-K. Liu, K. M. Shen, D. G. Schlom, Synthesis science of $SrRuO_3$ and $CaRuO_3$ epitaxial films with high residual resistivity ratios. *APL Mater.* **6**, 046101 (2018).
39. C. Domínguez, A. B. Georgescu, B. Mundet, Y. Zhang, J. Fowlie, A. Mercy, A. Waelchli, S. Catalano, D. T. L. Alexander, P. Ghosez, A. Georges, A. J. Millis, M. Gibert, J.-M. Triscone,

Length scales of interfacial coupling between metal and insulator phases in oxides. *Nat. Mater.* **19**, 1182–1187 (2020).

40. Z. Liao, N. Gauquelin, R. J. Green, K. Müller-Caspary, I. Lobato, L. Li, S. Van Aert, J. Verbeeck, M. Huijben, M. N. Grisolia, V. Rouco, R. El Hage, J. E. Villegas, A. Mercy, M. Bibes, P. Ghosez, G. A. Sawatzky, G. Rijnders, G. Koster, Metal–insulator-transition engineering by modulation tilt control in perovskite nickelates for room temperature optical switching. *Proc. Natl. Acad. Sci. U.S.A.* **115**, 9515–9520 (2018).
41. J. Fowlie, C. Lichtensteiger, M. Gibert, H. Meley, P. Willmott, J.-M. Triscone, Thickness-dependent perovskite octahedral distortions at heterointerfaces. *Nano Lett.* **19**, 4188–4194 (2019).
42. A. B. Georgescu, O. E. Peil, A. S. Disa, A. Georges, A. J. Millis, Disentangling lattice and electronic contributions to the metal-insulator transition from bulk vs. layer confined $RNiO_3$. *Proc. Natl. Acad. Sci. U.S.A.* **116**, 14434–14439 (2019).
43. S. Beck, G. Sclauzero, U. Chopra, C. Ederer, Metal-insulator transition in $CaVO_3$ thin films: Interplay between epitaxial strain, dimensional confinement, and surface effects. *Phys. Rev. B* **97**, 075107 (2018).
44. D. E. McNally, X. Lu, J. Pelliciari, S. Beck, M. Dantz, M. Naamneh, T. Shang, M. Medarde, C. W. Schneider, V. N. Strocov, E. V. Pomjakushina, C. Ederer, M. Radovic, T. Schmitt, Electronic localization in $CaVO_3$ films via bandwidth control. *npj Quantum Mater.* **4**, 6 (2019).
45. S. Koohfar, A. B. Georgescu, A. N. Penn, J. M. LeBeau, E. Arenholz, D. P. Kumah, Confinement of magnetism in atomically thin $La_{0.7}Sr_{0.3}CrO_3/La_{0.7}Sr_{0.3}MnO_3$ heterostructures. *npj Quantum Mater.* **4**, 25 (2019).
46. S. Koohfar, A. B. Georgescu, I. Hallsteinsen, R. Sachan, M. A. Roldan, E. Arenholz, D. P. Kumah, Effect of strain on magnetic and orbital ordering of $LaSrCrO_3/LaSrMnO_3$ heterostructures. *Phys. Rev. B* **101**, 064420 (2020).

## Acknowledgments

**Funding:** This work was primarily supported through the National Science Foundation (NSF) through the Platform for the Accelerated Realization, Analysis, and Discovery of Interface Materials (PARADIM) under Cooperative Agreement no. DMR-2039380 as well as grants no. DMR-1709255 and DMR-2104427. Additional support was provided through the Air Force Office of Scientific Research grants no. FA9550-15-1-0474 and FA9550-21-1-0168. J.N.N., N.J.S., and B.D.F. acknowledge support from the NSF Graduate Research Fellowship under grant no. DGE-1650441. C.T.P. acknowledges support from the Center for Bright Beams, NSF Award no. PHY-1549132 and from PARADIM (DMR-2039380). This research was also funded, in part, by the Gordon and Betty Moore Foundation's EPiQS Initiative through grant nos. GBMF3850 and GBMF9073 to Cornell University. Substrate preparation was performed, in part, at the Cornell NanoScale Facility, a member of the National Nanotechnology Coordinated Infrastructure (NNCI), which is supported by the NSF (grant no. NNCI-2025233). This work made use of the Cornell Center for Materials Research Shared Facilities, which are supported through the NSF MRSEC program (DMR-1719875). The FEI Titan Themis 300 was acquired through no. NSF-MRI-1429155, with additional support from Cornell University, the Weill Institute, and the Kavli Institute at Cornell. The Thermo Fisher Helios G4 UX FIB was acquired with support by NSF no. DMR-2039380. The Flatiron Institute is a division of the Simons Foundation. **Author contributions:** J.N.N. performed the ARPES measurements with assistance from N.J.S. and guidance from K.M.S. J.N.N. and N.J.S. synthesized the thin films with guidance from D.G.S. A.B.G. performed the DFT calculations with guidance from A.G. and A.J.M. B.H.G. performed the STEM imaging with guidance from L.F.K. B.D.F. performed the in situ van der Pauw transport measurements and, along with C.T.P, assisted in the acquisition of photoemission data. C.Z. assisted with the sample characterization. A.B.G., A.J.M., and A.G. helped to pose the problem. J.N.N. and K.M.S. conceived the project and wrote the manuscript with contributions from all authors. K.M.S. supervised the project. **Competing interests:** The authors declare that they have no competing interests. **Data and materials availability:** All data needed to evaluate the conclusions in the paper are present in the paper and/or the Supplementary Materials.

Submitted 27 April 2021
Accepted 13 December 2021
Published 4 February 2022
10.1126/sciadv.abj0481

Science Advances

# Interfacial charge transfer and persistent metallicity of ultrathin SrIrO$^3$/SrRuO$^3$ heterostructures

Jocienne N. NelsonNathaniel J. SchreiberAlexandru B. GeorgescuBerit H. GoodgeBrendan D. FaethChristopher T. ParzyckCyrus ZeledonLena F. KourkoutisAndrew J. MillisAntoine GeorgesDarrell G. SchlomKyle M. Shen

*Sci. Adv.*, 8 (5), eabj0481. • DOI: 10.1126/sciadv.abj0481

---

*Science Advances* (ISSN ) is published by the American Association for the Advancement of Science. 1200 New York Avenue NW, Washington, DC 20005. The title *Science Advances* is a registered trademark of AAAS.